Maturation stages of glauconites: a combined electron microprobe, Raman, and thermogravimetric study

Davide Lenaz[1], Stefano Giovanoni[1], Francesco Parrino[2], Danilo Bersani[3], Filippo Parisi[1]*

[1]Dipartimento di Matematica e Geoscienze, Università degli studi di Trieste, via Weiss 8, 34122 Trieste, Italy

[2]Dipartimento di Ingegneria Industriale, Università degli studi di Trento, via Sommarive 9, 38123 Trento, Italy

[3]Dipartimento di Scienze Matematiche, Fisiche e Informatiche, Università degli studi di Parma, Parco Area delle Scienze 7A, 43124 Parma, Italy

Abstract Glauconite mineral is one of the most sensitive indicators of low sedimentation rate in the marine environment. The time of residence of glauconites at the sea bottom before burial is reflected by their so-called maturity that is differentiated based on their K_2O content.

The present work aims to investigate the evolution of glauconites during the transition toward the highly evolved level. Complementary electron microprobe, Raman, and Thermogravimetric analysis were performed on glauconitic grains from the Belluno basin (N Italy) with different K_2O content in order to verify whether the level of glauconites evolution affects the results of these surveys.

The obtained results show that Raman spectra are sensitive to the grade of glauconite maturations. First, spectra of mature glauconites are more structured, due to the lower degree of Al substitution in the octahedral sites.

Moreover, the position of the strongest Raman peak (Si–Ob–Si mode) at ~700 cm^{-1} shows two contrasting behaviors in the early (K_2O <8%) and late (K_2O> 8%) stages of glauconites maturation,

respectively. TGA measurements reveals that the presence of interlayer water is also related to the state of glauconites maturations. The obtained results were explained in the light of different isomorphic substitutions occurring at octahedral level in the mature and non-mature glauconites, thus allowing to obtain a deeper insight onto the mechanism of glauconites evolution.

Key words: glauconite; potassium content; Raman spectroscopy; TGA; EMPA

Introduction

Among the different indicators of low sedimentation rate in marine environments, glaucony is one of the most sensitive and includes green marine grains with a considerable variability [1] from iron-rich 2:1 dioctahedral minerals (interlayered glauconite-smectite; [2]) to glauconite *s.s.*, with a great proportion of potassium as interlayer cation [3,4]. After Odin and Matter (1981) and Amorosi (1995, 1997) [5–8], glauconitic grains are collectively defined as glaucony while the term glauconite is used only for the K-rich end-member of the glauconitic mineral family.

According to Odin and Matter (1981) [5] and Odin and Fullagar (1988) [9], the glauconitization processes include a two-stage model: i) the formation of a K-poor, Fe^{3+}-rich smectite precursor (possibly due to microbial activity;[10–12]) and ii) a gradual enrichment with K^+ to form a K-rich glauconitic mica. It is to notice, however, that according to other researchers [13,14] other phyllosilicates minerals can be considered as a precursor such as a glauconitic clay or a kaolinite-smectite bearing substratum.

The time of residence of glauconites at the sea bottom before burial is reflected by their so-called maturity. Based upon composition and structure of glauconitic minerals, four stages of evolution have been differentiated: nascent (K_2O 2-4 wt.%), slightly evolved (K_2O 4-6 wt.%), evolved (K_2O 6-8 wt.%), highly evolved (K_2O > 8 wt.%) [5–9,15,16]. In order to define the evolution of glauconies several techniques have been used as electron microprobe, powder X-ray diffraction investigating the distance between the peaks (001) and (020) [8,9,17] and magnetic characterization

[18]. Amorosi et al. [8] noted that "The outstanding advantage of characterizing glaucony by its paramagnetic susceptibility, in spite of lack of accurate determination, is that magnetic separation is easy to perform and inexpensive" however "it is recommended that analysis of magnetic properties [should] be used in conjunction with other methods, such as geochemical and diffractometrical analyses". To shed light on the mechanism involved in the glauconitization process, different authors [19–22], performed HRTEM analyses. Amouric and Parron (1985) [19] found out smectite-rich and glauconite packets but no interlayering. Buatier et al. (1989) [20] found out that glauconite crystallites are commonly parallel to smectite layers forming an irregular "interstratified" sequence. Jiménez-Millán et al. (1998) [21] did not observe a textural relationship between smectite and glauconite. López-Quirós et al. (2020)[22] revealed the occurrence of individual smectite layers between the glauconite packets.

Despite the copious literature in the field, the processes involved during the evolution stages of glauconites are still not fully understood and continues to attract a high level of research interest.

For its straightforward use in the material characterisation of hard matter, Raman spectroscopy is now an eminent technique [23,24]. Previous Raman analyses on glauconites have been performed especially on green pigments in order to recognize them from celadonites, smectites, chlorites, serpentines and malachite [25–29]. As explained before, however, the main purpose for these last works was to discriminate different green-coloured phases, so that they did not enter in a great detail.

A chemistry-dependent Raman study on glauconite was been published by Baumgartner et al. in 2022 [30] but a systematic study on the changes occurring in Raman spectra during the maturation processes is still lacking. The main objective of the present study was to investigate the variations occurring in chemical compositions and in Raman spectra as a function of the maturity stage. The potential role of adsorbed and interlayer water molecules can also be considered by performing thermogravimetric analysis.

In the light of these considerations, complementary electron microprobe, Raman and thermogravimetric analysis were performed on glauconitic grains from the Belluno Glauconite Arenite formation with K_2O content in the range 5-10 wt. %. The correlation between the results of the different analyses provides important information, relating to the octahedral isomorphic substitutions, useful to obtain a deeper insight into the mechanism of glauconites maturation.

Materials and methods

The Veneto-Friuli Chattian to Messinian molasse basin is located at the junction of three orogenic belts, the Dinarides, Alps and the Apennines-Southern Alps system, the former two being characterized by an orogenic acme in the Paleogene, the latter in the Neogene (Fig. 1A). The molasse is a clastic wedge up to 4000 meters thick, trending WSW-ENE showing maximum thickness at the boundary between the eastern Southern Alps and the Veneto-Friuli plain and gradually wedges out southwards. Significant contributions dealing with several aspects of the Veneto-Friuli molasse were given by Cason et al. (1981), Cousin (1981), Massari (1983, 1984), Stefani (1982, 1984) and Massari et al. (1986) [31–36].

The fill of the molasse basin can be subdivided into minor and major sequence often bounded at the base by glauconitic beds marking eustatic or regionally significant sea-level changes. A number of glauconitic layers are of limited extent and genetically linked to locally developed clastic progradational units. The reworking of relict sediments occurs on a limited scale and the glauconitic sheet-sand can be considered an abandonment facies deposited after a definite deltaic episode.

In general, the glauconitic layers show a massive bedding. The amount of glauconite and abundance of fossils varies from sparse in marginal facies to very abundant in more open marine facies. According to Massari et al. (1986) [37] a significant difference exists between Chattian-Langhian petrofacies, with a spectrum ranging from sublitharenites to litharenites with more than fifty per

100 cent of quartz, and Serravallian-Messinian petrofacies with litharenites dominated by extrabasinal
101 carbonate clasts (Fig. 2A and B).

102

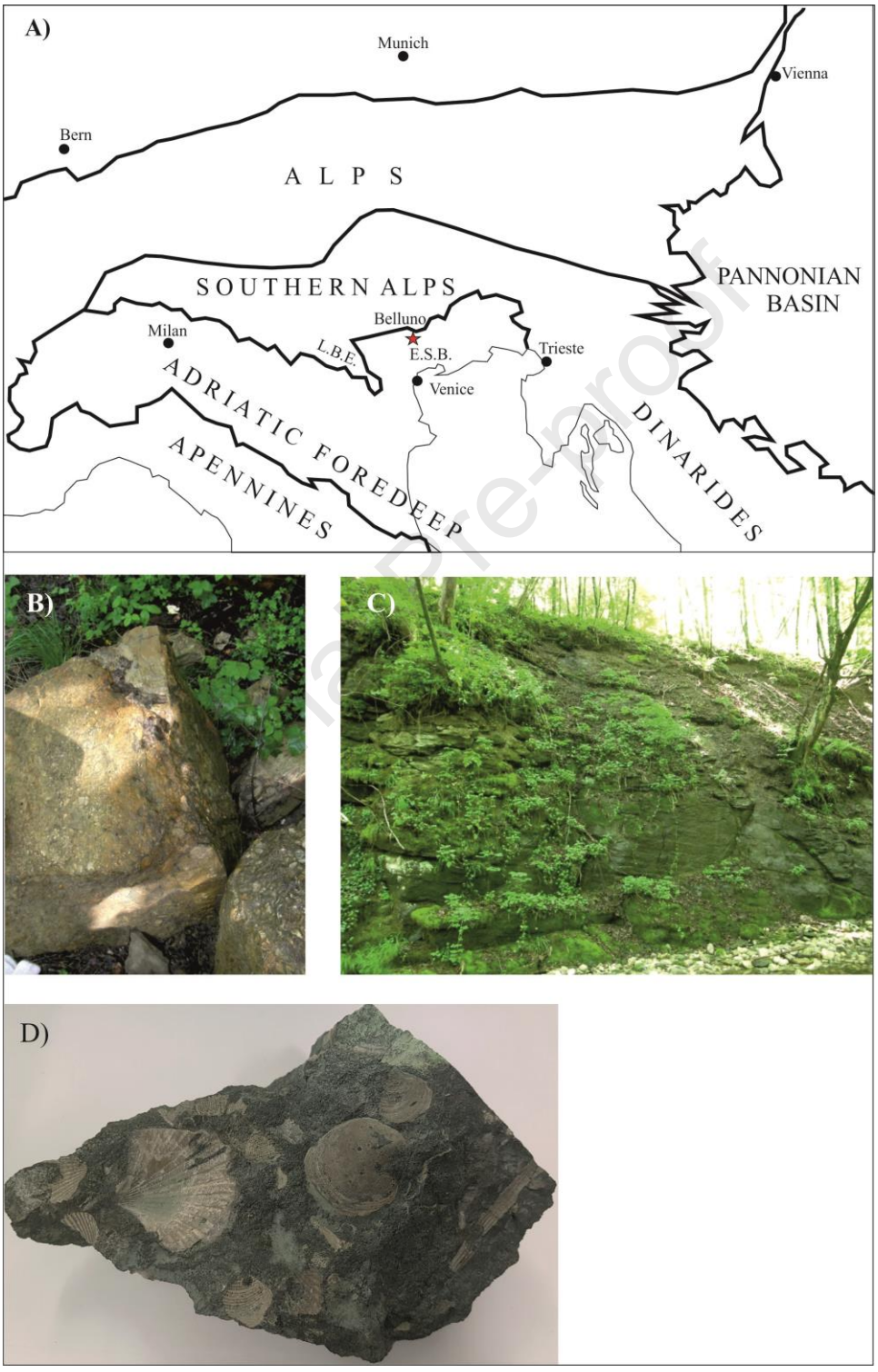

103

Fig. 1. **A)** Simplified sketch-map showing the position of the eastern South-Alpine molasse basin (ESB) with respect to the adjoining orogenic belts (after Massari et al., 1986). LBE: Lessini-Berici-Euganei high; **B)** outcrop for sample GB2; **C)** outcrop for sample GB4; **D)** hand specimen for sample GB1.

We sampled 7 glauconitic beds (labelled as GB1-GB7) around Belluno city (Fig. 1B, C, D), crashed them and concentrated glauconitic grains by means of a Frantz isodynamic magnetic separator (Fig. 2C). Glauconitic grains of different size and colour (pale to dark green) have been handpicked under the microscope, put on an adhesive tape, embedded in epoxy resin and polished. About 120 glauconite grains have been analysed using a CAMECA-SX50 electron microprobe (EMPA) at IGG-CNR Padua, operating at 15 kV and 15 nA. A 20 s counting time was used for both peak and total background. Among the complete set of analysed samples, two of them (GB4 and GB6) showed glauconitic grains with considerable chemical variations among grains (K_2O 5-10 wt.%). The same glauconitic grains from these samples have been successively analysed by Raman spectroscopy. In such a way we were certain of the absence of other phases but glauconites. No other phases have been recognised via EMPA and Raman analyses. Thermogravimetry (TG) measurements have been performed on samples constituted by several grains from the same glauconitic beds.

The micro-Raman measurements were performed with a Jobin–Yvon Labram apparatus, equipped with holographic notch filter, motorized *xy* stage, auto-focus and microscope Olympus BH-4. The objective 100× with a spatial resolution of about 1 μm was used for the measurements. The light at 632.8 nm of a HeNe laser (maximum power 20mW) was used for excitation. The laser power on the sample was kept lower than 1 mW using a series on neutral density filters. The spectral resolution is ~2cm^{-1}. The typical measurement was a series of 5 accumulations of 60 seconds each. The accuracy on the position and width of the Raman bands, obtained by means of Gauss-Lorentzian fitting using the LabSpec 5 software, is 0.5 cm^{-1} (it can be worse for weak and broad bands).

TG measurements were performed by means of a Q5000 IR apparatus (TA Instruments) under the nitrogen flow of 10 cm^3 min^{-1} for the sample and 10 cm^3 min^{-1} for the balance. The weight of each sample was ca. 10 mg. The experiments were performed by heating the sample from ca. 30 to 400 °C with a rate of 10 °C min^{-1}. The temperature calibration was carried out by means of the Curie temperatures of provided standards.

Results and discussion.

The results of electron-microprobe analysis (EMPA) on glauconitic grains showed that the main oxides are SiO_2 (51-58 wt. %), FeO_{tot} (20-30 wt. %), K_2O (5.8-9.5 wt. %), Al_2O_3 (3-9 wt. %) and MgO (5-7 wt. %). Calcium oxide is present in variable amount, but sometimes its presence can be due to calcareous particles within the grains so that we arbitrarily considered only grains with CaO lower than 2 wt. %. Other oxides such as Na_2O, TiO_2 and MnO are lower than 0.4 wt. %.

Chemistry reveals that within the different layers sampled there are two layers (GB4 and GB6) where the range of K_2O is rather spread covering almost the entire range of K_2O registered in this study, while in the other layers the range is much narrower.

Given this, we decided to focus on these two samples (Fig.1) and to perform Raman and thermal analysis on glauconites from these two layers.

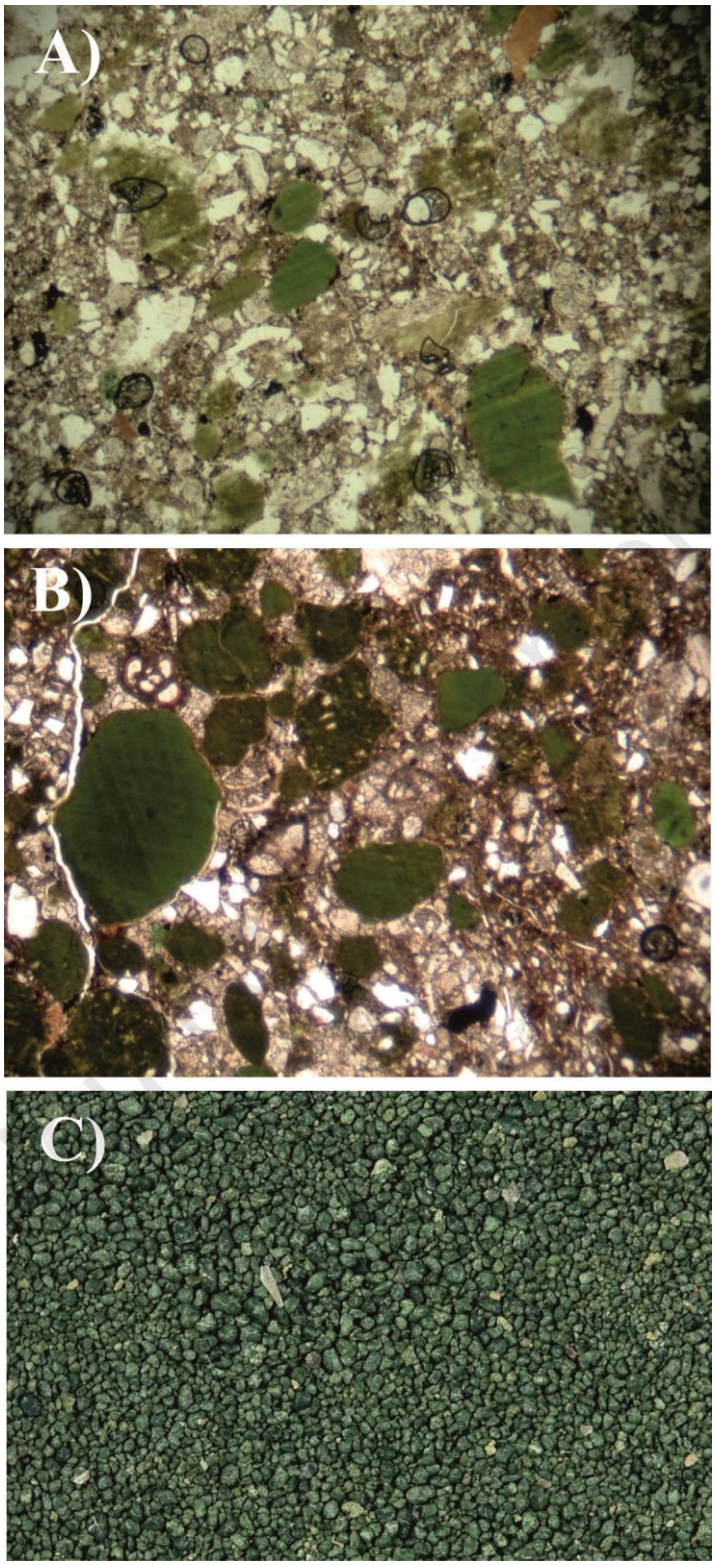

Fig. 2. A) Thin sections of GB1and **B)** GB6 samples showing the glauconitic grains. **C)**: glauconite grains after magnetic concentration

Compositional changes due to evolution processes are illustrated in Fig. 3 where the relations between K_2O and magnesium, aluminium and iron oxides are reported.

153

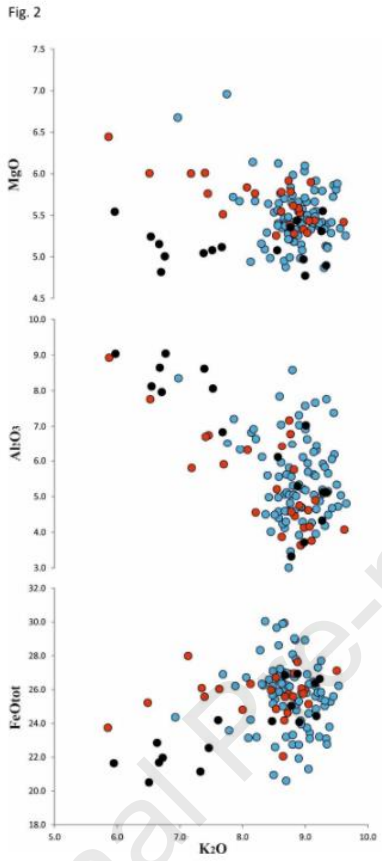

154

155 **Fig. 3.** MgO, Al_2O_3 and FeO_{tot} vs. K_2O diagrams. Red circle: GB4 glauconites; black circles: GB6
156 glauconites; blue circles: glauconites from other layers of the Belluno Basin.

157

158 Figure 3 evidences that both Al_2O_3 and MgO percentages decrease on increasing K_2O content,
159 while a weak positive relation between FeO_{tot} and K_2O can be observed.

160 It is reasonable to suppose that the higher content in K^+ into the clay interlayer is balanced by
161 isomorphic substitutions in the octahedral sites between trivalent aluminum and divalent iron (Al^{3+}
162 $\rightarrow Fe^{2+}$). The decrease in Mg^{2+} takes account of the isomorphic substitutions in the octahedral sites
163 between divalent Mg^{2+} and trivalent Fe^{3+} ($Mg^{2+} \rightarrow Fe^{3+}$).

164 This last process is significant only at the early stages of glauconites maturations, as confirmed
165 from the observation that the Mg^{2+} loss is more pronounced at lower K_2O content (< 8%).

166 The proposed considerations are in accordance with the results of López-Quirós et al (2020) [22]
167 which found that more mature glauconite grains are characterized by major K^{+} and Fe^{2+} and minor
168 Fe^{3+} content and that potassium is stabilized at the interlayer site by the octahedrally coordinated
169 Fe^{2+}.

170 Typical Raman spectra of glauconitic grains at different evolution stages are reported in Figure 4.

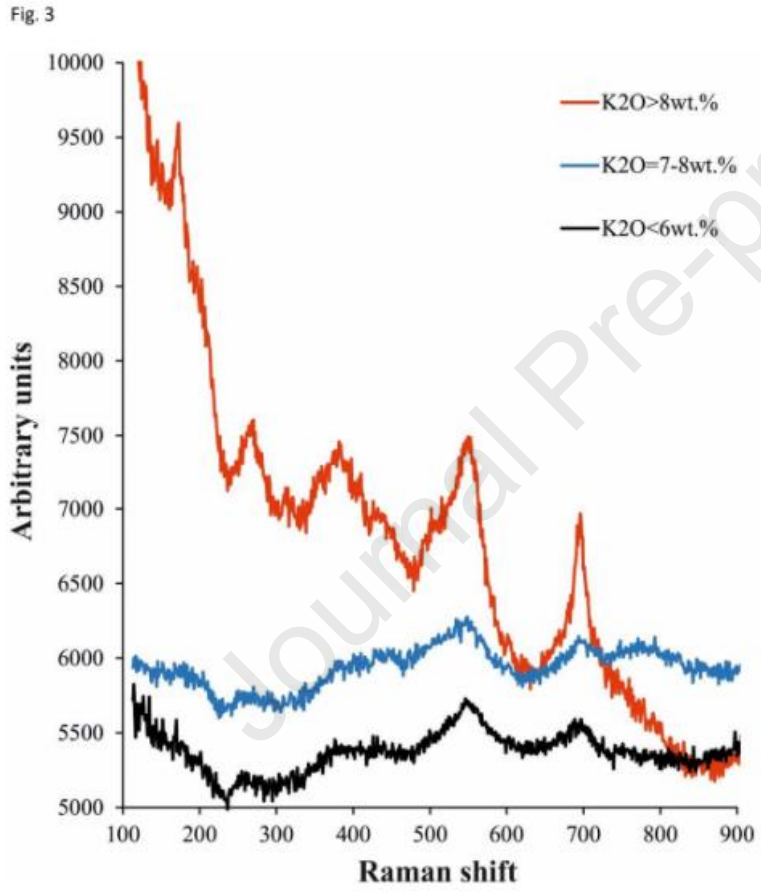

171

172 **Fig. 4.** Raman spectra of glauconites with K_2O content lower than 6 wt. % (black line), in the range
173 7-8 wt. % (blue line) and higher than 8 wt. % (red line).

174

175 A review of literature data [25,26,38] showed that the Raman spectra of glauconitic grains presents
176 characteristic bands in the range 100–800 cm^{-1}, while at higher wave-numbers only broad weak
177 bands are sometimes visible. Grissom (1986) assigned those broad peaks to the hydroxyl stretching

178 (3610 and 3545 cm^{-1}), the hydroxyl bending (1630 cm^{-1}) and the Si-O stretching (970 and 1110 cm^{-1}
179). In the present study we did not consider the frequency zone higher than 800 cm^{-1}, because, given
180 the above assignments, they should be not related to the K_2O content.
181 The presence of the glauconites characteristic bands [25,39,40] at ~ 190, 260, 390, 440, 550 and
182 700 cm^{-1} is clearly observed in the Raman spectrum of highly evolved glauconites (K^+ content
183 higher than 8%).
184 As for the less evolved glauconites grains (K content lower than 8%), in the low-wavenumber
185 spectral region, the poor resolution of the Raman peaks does not allow to establish the exact
186 position of bands. According to Ospitali et al. 2008 [25] this spectral region is related to the internal
187 vibrations of the MoO6 octahedra (Mo = interlayer metal atom)
188 It is reasonable to suppose that Raman spectra of mature glauconites are more structured due to the
189 lower degree of Al substitution in the octahedral sites which lead to a more ordered structure and
190 consequently to narrower and more resolved peaks. This effect is confirmed by Fig. 5 where the
191 negative correlation between the Full Width at Half Maximum (FWHM) of the peak in the range
192 690-700 cm^{-1} and the K_2O content, is reported.
193

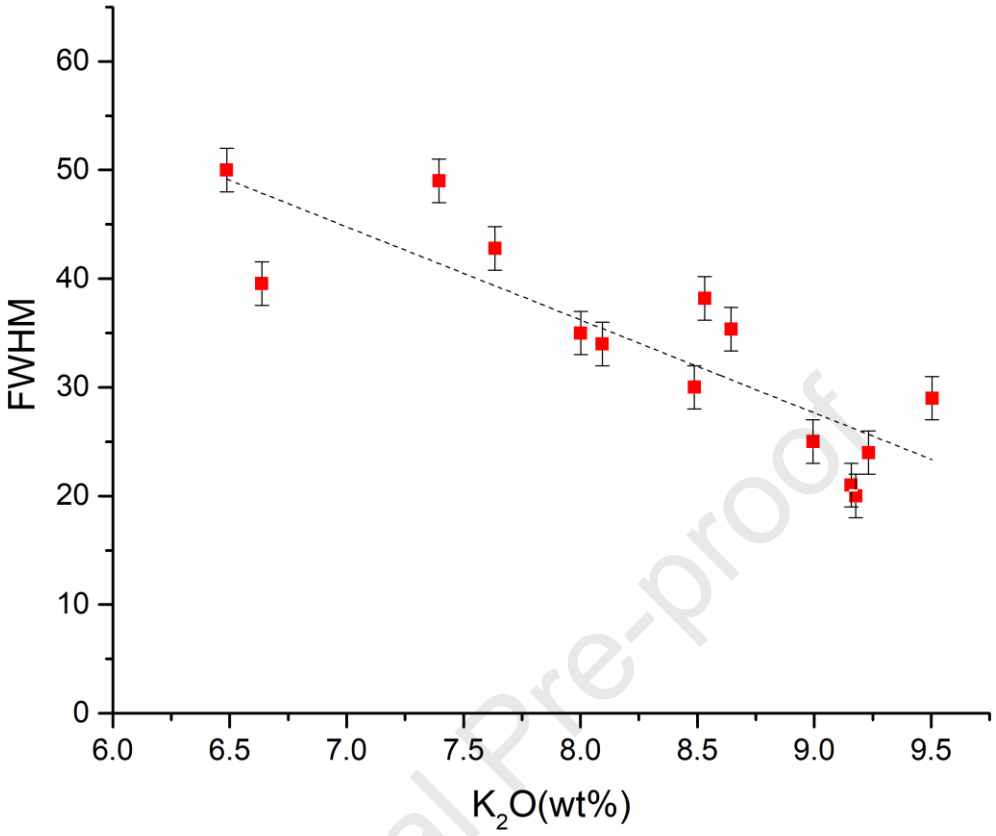

194

195

196 **Fig. 5.** Full Width at Half Maximum (FWHM) of the peak in the range 690-700 cm^{-1} vs. K_2O wt.%.

197

198 In the 450-800 cm^{-1} spectral region, related to the vibrations mode of the SiO_4 tetrahedra [25,41],
199 well-defined peaks at ~ 550 (δSi-O-R and δR-O-H, with R = octahedral ion,) and 700 cm^{-1} (νSi–
200 Ob–Si) are observed.

201 Aiming at evaluating the influence of the evolution stage on the Raman spectra, the eventual
202 occurrence of changes in the position of the peaks at ~ 550 and 700 cm^{-1}, on varying chemical
203 composition, was investigated.

As for the Si-O-R and R-O-H bending (550 cm^{-1}), our experiments showed no correlation with chemical composition, while the position of the strongest Raman peak (Si–Ob–Si mode) at ~700 cm^{-1} shows a peculiar behaviour.

As observed in Fig. 6 the values of frequencies increase in the early stages of glauconites maturation, until the K_2O content reaches the value of 8%, then a negative correlation between the Raman shift and the K_2O content is observed.

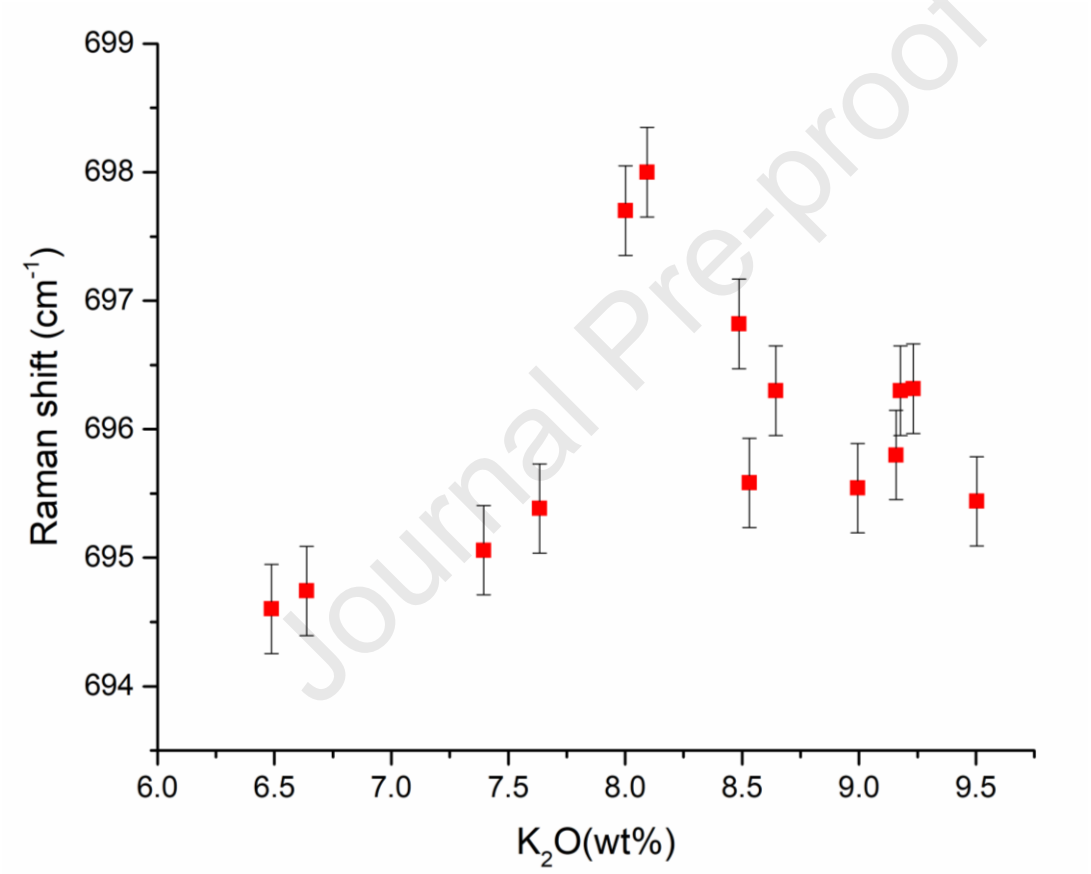

Fig. 6. Raman shift of the strong peak in the range 547-553 cm^{-1} vs. K_2O wt.% for the glauconites.

As reported in (Wang, Freeman, e Jolliff 2015), the major factors that influences this Raman peak positions, in phyllosilicates, is the difference in effective ionic radii [42] among octahedral cations, i.e., Al^{3+} (0.535 Å), Fe^{3+} (0.645 Å), Mg^{2+}(0.72 Å), and Fe^{2+} (0.78 Å). The length of the M-O bond in octahedral sites is shorter in the case of high content of trivalent ions, thus producing higher

Raman shift values, while it is higher where bigger divalent cations are located, thus producing lower frequency values.

In the present case, the Raman shift of the νSi–Ob–Si peak is always below 700 cm^{-1}, which is probably due to the low content of Al^{3+} and Fe^{3+} compared to Fe^{2+} and Mg^{2+} ions.

The data reported in Figure 5 can be explained considering the different isomorphic substitution that occurs at octahedral level in the mature and non-mature glauconites.

In the early stages of maturation, both $Mg^{2+} \rightarrow Fe^{3+}$ and $Al^{3+} \rightarrow Fe^{2+}$ substitutions probably occur. The first process should lead to an increase of the frequency values (because the Fe^{3+}−O bonds are shorter), while the other process should lead to lower Raman shift values (due to the longer Fe^{2+}−O bonds).

The observation that the νSi–Ob–Si increases at the beginning of the maturation process seems to indicate that the first effect prevails.

The opposite trend, observed for the highly evolved glauconites, can be explained by considering that, the high K^{+} content requires the expulsion of trivalent cations and an increase of the divalent ones (mainly Fe^{2+}) at the octahedral level.

We can finally conclude that Raman spectra are sensitive to the grade of glauconite maturations in terms of both resolution of Raman peaks in the low-wavenumber region and in terms of shift of the Raman frequencies around 700cm^{-1}. The opposite trends observed for this peak as a function of the maturation stage, give important information about the exchange process occurring at the octahedral level.

To further investigate the behaviour of glauconites as a function of their maturation state TGA measurements were performed. Thermogravimetric analysis is frequently employed to characterize water content and thermal stability of many kinds of minerals [43–48]. The thermograms shown in Fig. 7 refers to three different samples with three different K_2O content.

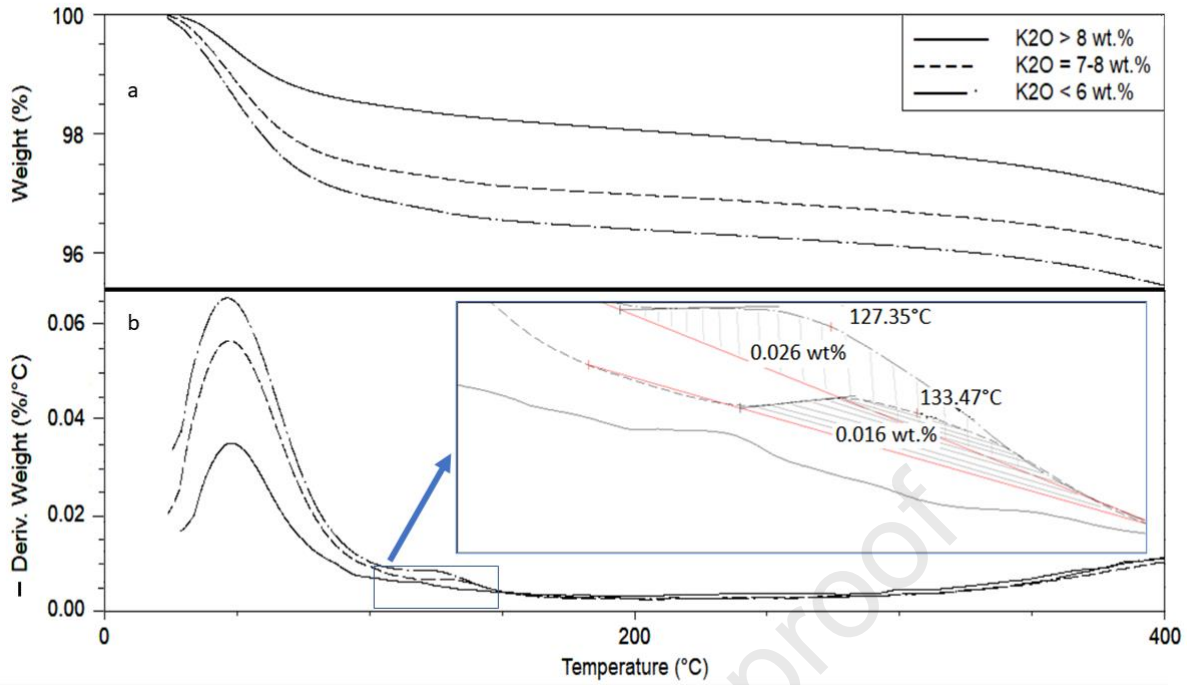

Fig. 7. TG (a) and DTG (b) curves of three different glauconite samples.

The TG diagrams seem to show only a pronounced weight loss due to the loss of adsorbed water, while in the DTG curves, they show two losses. The first from 30 to 100 degrees, which is most likely adsorbed water [Fernandez-Landero et al.). The second (more visible in the inset), with a maximum at ca.130 C° which is most likely interlayer water. Note the negative relationship between the amount of water in the interlayer and the maturity of glauconite. This relationship seems to be easily explained by the fact that, as the K^+ concentration of the interlayer increases, the interlayer water decreases.

Conclusions

A combined EMPA, Raman and TGA study was performed in order to investigate the evolution stages of glauconites during the transition toward the highly evolved level. Considering that the transition from nascent to highly evolved glauconites is supposed to be the following: Microbial oxidation → Formation of Fe^{3+}-smectite → Fe^{3+}-smectite to glauconite reaction [5,12]. Our work

suggests a lowering of the water content driven by increased interlayer content of K^+ in the last evolution stage from evolved to highly evolved glauconites. The obtained results show that Raman spectra are sensitive to the grade of glauconite maturations. The spectra of mature glauconites are more structured, due to the lower degree of Al substitution in the octahedral sites and lower water content.

Moreover, the position of the strongest Raman peak (Si–Ob–Si mode) at ~700 cm^{-1} shows two contrasting behaviours. In the early (K_2O <8%) stages the Al and Mg^{2+} in the octahedral site is replaced by $Fe^{2+}$and Fe^{3+}. In the late (K_2O> 8%) stages of glauconites maturation the Al is replaced by Fe^{2+}. The opposite trends observed for this peak as a function of the maturation stage, give important information about the exchange process occurring at the octahedral level.

Acknowledgements

DL thanks R. Carampin (C.N.R. Padua), L. Furlan (Trieste University) and L. Tauro (Padua University) for technical support. This work was part of the M.Sc. thesis of SG.

References

[1] S. Banerjee, U. Bansal, K. Pande, S.S. Meena, Compositional variability of glauconites within the Upper Cretaceous Karai Shale Formation, Cauvery Basin, India: Implications for evaluation of stratigraphic condensation, Sediment. Geol. 331 (2016) 12–29. https://doi.org/10.1016/j.sedgeo.2015.10.012.

[2] B. Velde, Further Information Related to the Origin of Glauconite, Clays Clay Miner. 23 (1975) 376–381. https://doi.org/10.1346/CCMN.1975.0230509.

[3] S.W. Bailey, Summary of recommendations of AIPEA nomenclature committee, Clay Miner. 15 (1980) 85–93. https://doi.org/10.1180/claymin.1980.015.1.07.

[4] I.E. Odom, 13. GLAUCONITE and CELADONITE MINERALS, in: S.W. Bailey (Ed.), Micas, De Gruyter, 1984: pp. 545–572. https://doi.org/10.1515/9781501508820-017.

[5] G.S. Odin, A. Matter, De glauconiarum origine, Sedimentology. 28 (1981) 611–641. https://doi.org/10.1111/j.1365-3091.1981.tb01925.x.

[6] A. Amorosi, Detecting compositional, spatial, and temporal attributes of glaucony: a tool for provenance research, Sediment. Geol. 109 (1997) 135–153. https://doi.org/10.1016/S0037-0738(96)00042-5.

[7] A. Amorosi, I. Sammartino, F. Tateo, Evolution patterns of glaucony maturity: A mineralogical and geochemical approach, Deep Sea Res. Part II Top. Stud. Oceanogr. 54 (2007) 1364–1374. https://doi.org/10.1016/j.dsr2.2007.04.006.
[8] Alessandro Amorosi, Glaucony and Sequence Stratigraphy: A Conceptual Framework of Distribution in Siliciclastic Sequences, SEPM J. Sediment. Res. Vol. 65B (1995). https://doi.org/10.1306/D4268275-2B26-11D7-8648000102C1865D.
[9] G.S. Odin, P.D. Fullagar, Chapter C4 Geological Significance of the Glaucony Facies, in: Dev. Sedimentol., Elsevier, 1988: pp. 295–332. https://doi.org/10.1016/S0070-4571(08)70069-4.
[10] A. Gaudin, M.D. Buatier, D. Beaufort, S. Petit, O. Grauby, A. Decarreau, Characterization and origin of Fe³⁺-montmorillonite in deep-water calcareous sediments (Pacific Ocean, Costa Rica margin), Clays Clay Miner. 53 (2005) 452–465. https://doi.org/10.1346/CCMN.2005.0530503.
[11] D. Charpentier, M.D. Buatier, E. Jacquot, A. Gaudin, C.G. Wheat, Conditions and mechanism for the formation of iron-rich Montmorillonite in deep sea sediments (Costa Rica margin): Coupling high resolution mineralogical characterization and geochemical modeling, Geochim. Cosmochim. Acta. 75 (2011) 1397–1410. https://doi.org/10.1016/j.gca.2010.11.026.
[12] A. Baldermann, L.N. Warr, G.H. Grathoff, M. Dietzel, The Rate and Mechanism of Deep-Sea Glauconite Formation at the Ivory Coast – Ghana Marginal Ridge, Clays Clay Miner. 61 (2013) 258–276. https://doi.org/10.1346/CCMN.2013.0610307.
[13] P. Stille, N. Clauer, The process of glauconitization: chemical and isotopic evidence, Contrib. Mineral. Petrol. 117 (1994) 253–262. https://doi.org/10.1007/BF00310867.
[14] E. Galán, I. González, E. Mayoral, F. Muñiz, Contribution of clay mineralogy to the paleoenvironmental interpretation of upper Miocene detrital sediments, Euroclay95 Leuven Abstr. 1 (1993) 311–312.
[15] Y.K. Bentor, ed., Marine Phosphorites: Geochemistry, Occurrence, Genesis, SEPM (Society for Sedimentary Geology), 1980. https://doi.org/10.2110/pec.80.29.
[16] P. Giresse, M. Lamboy, G. Odin, Évolution géométrique des supports de glauconitisation ; application à la reconstitution de paléoenvironnement, (1980) application/pdf true.
[17] G.S. Odin, Significance of Green Particles (Glaucony, Berthierine, Chlorite) in Arenites, in: G.G. Zuffa (Ed.), Proven. Arenites, Springer Netherlands, Dordrecht, 1985: pp. 279–307. https://doi.org/10.1007/978-94-017-2809-6_13.
[18] G. Odin, How to measure glaucony ages, (1982).
[19] M. Amouric, Structure and Growth Mechanism of Glauconite as Seen by High-Resolution Transmission Electron Microscopy, Clays Clay Miner. 33 (1985) 473–482. https://doi.org/10.1346/CCMN.1985.0330601.
[20] M. Buatier, Fe-Smectite-Glauconite Transition in Hydrothermal Green Clays from the Galapagos Spreading Center, Clays Clay Miner. 37 (1989) 532–541. https://doi.org/10.1346/CCMN.1989.0370605.
[21] J. Jimenez-Millan, J.M. Molina, F. Nieto, L. Nieto, P.A. Ruiz-Ortiz, Glauconite and phosphate peloids in Mesozoic carbonate sediments (Eastern Subbetic Zone, Betic Cordilleras, SE Spain), Clay Miner. 33 (1998) 547–559. https://doi.org/10.1180/000985598545886.
[22] A. López-Quirós, A. Sánchez-Navas, F. Nieto, C. Escutia, New insights into the nature of glauconite, Am. Mineral. 105 (2020) 674–686. https://doi.org/10.2138/am-2020-7341.
[23] D. Lenaz, V. Lughi, Raman spectroscopy and the inversion degree of natural Cr-bearing spinels, Am. Mineral. 102 (2017) 327–332. https://doi.org/10.2138/am-2017-5814.
[24] V. Lughi, D. Lenaz, A. Bonifacio, F. Princivalle, V. Sergo, F. Parisi, A Raman spectroscopy study of the oxidation processes in synthetic chromite FeCr2O4, Ceram. Int. 46 (2020) 29382–29387. https://doi.org/10.1016/j.ceramint.2020.07.059.

[25] F. Ospitali, D. Bersani, G. Di Lonardo, P.P. Lottici, 'Green earths': vibrational and elemental characterization of glauconites, celadonites and historical pigments, J. Raman Spectrosc. 39 (2008) 1066–1073. https://doi.org/10.1002/jrs.1983.
[26] I. Aliatis, D. Bersani, E. Campani, A. Casoli, P.P. Lottici, S. Mantovan, I.-G. Marino, F. Ospitali, Green pigments of the Pompeian artists' palette, Spectrochim. Acta. A. Mol. Biomol. Spectrosc. 73 (2009) 532–538. https://doi.org/10.1016/j.saa.2008.11.009.
[27] L.M. Moretto, E.F. Orsega, G.A. Mazzocchin, Spectroscopic methods for the analysis of celadonite and glauconite in Roman green wall paintings, J. Cult. Herit. 12 (2011) 384–391. https://doi.org/10.1016/j.culher.2011.04.003.
[28] V. Košařová, D. Hradil, I. Němec, P. Bezdička, V. Kanický, Microanalysis of clay-based pigments in painted artworks by the means of Raman spectroscopy: Raman spectroscopy of clay-based pigments, J. Raman Spectrosc. 44 (2013) 1570–1577. https://doi.org/10.1002/jrs.4381.
[29] J.L. Perez-Rodriguez, M. del C.J. de Haro, B. Siguenza, J.M. Martinez-Blanes, Green pigments of Roman mural paintings from Seville Alcazar, Appl. Clay Sci. 116–117 (2015) 211–219. https://doi.org/10.1016/j.clay.2015.03.016.
[30] R.J. Baumgartner, J. Cuadros, J. Michalski, B. Pejcic, C. Laukamp, S. Hu, J. Bourdet, Chemistry-dependent Raman spectral features of glauconite and nontronite: Implications for mineral identification and provenance analysis, Am. Mineral. 107 (2022) 1080–1090. https://doi.org/10.2138/am-2022-8044.
[31] C. Cason, Depositi deltizi nella molassa Cattiano-Burdigaliana del Bellunese (Alpi meridionali), Società cooperativa tipografica, 1980. https://books.google.it/books?id=A-fGXwAACAAJ.
[32] F. Massari, Tabular Cross-Bedding in Messinian Fluvial Channel Conglomerates, Southern Alps, Italy, in: J.D. Collinson, J. Lewin (Eds.), Mod. Anc. Fluv. Syst., Blackwell Publishing Ltd., Oxford, UK, 1983: pp. 287–299. https://doi.org/10.1002/9781444303773.ch23.
[33] C. Stefani, Geologia dei dintorni di Fanna e Cavasso Nuovo (Prealpi Carniche)., Mem. Sci. Geol. 35 (1982) 203–212.
[34] C. Stefani, Sedimentologia della molassa delle Prealpi Carniche occidentali, Mem. Sci. Geol. 36 (1984) 427–442.
[35] M. Cousin, Les rapports Alpes-Dinarides. Les confins de I'Italie et de la Yougoslavie. Société Géologique du Nord, Publication, Société géologique du nord (1981), 1-521, n.d.
[36] F. Massari, Resedimented Conglomerates of a Miocene Fan-Delta Complex, Southern Alps, Italy, In: E.H. Koster and R.Y. Steel, Eds., Sedimentology of gravels and conglomerates. Canadian Society of Petroleum Geologists Memoir 10 (1984), 259-277, (n.d.).
[37] F. Massari, P. Grandesso, C. Stefani, A. Zanferrari, The Oligo-Miocene Molasse of the Veneto-Friuli region, Southern Alps, G. Geol. 48 (1986) 235–255.
[38] A.M. Correia, R.J.H. Clark, M.I.M. Ribeiro, M.L.T.S. Duarte, Pigment study by Raman microscopy of 23 paintings by the Portuguese artist Henrique Pousão (1859–1884), J. Raman Spectrosc. 38 (2007) 1390–1405. https://doi.org/10.1002/jrs.1786.
[39] F. Nieto, I. Abad, B. Bauluz, M. Reolid, Textural and genetic relationships between glauconite and celadonite at the nanoscale: two different structural-compositional fields, Eur. J. Mineral. 33 (2021) 503–517. https://doi.org/10.5194/ejm-33-503-2021.
[40] A. Wang, J.J. Freeman, B.L. Jolliff, Understanding the Raman spectral features of phyllosilicates, J. Raman Spectrosc. 46 (2015) 829–845. https://doi.org/10.1002/jrs.4680.
[41] A. Wang, J.J. Freeman, B.L. Jolliff, Understanding the Raman spectral features of phyllosilicates: Raman spectral features of phyllosilicates, J. Raman Spectrosc. 46 (2015) 829–845. https://doi.org/10.1002/jrs.4680.

[42] R.D. Shannon, Revised effective ionic radii and systematic studies of interatomic distances in halides and chalcogenides, Acta Crystallogr. Sect. A. 32 (1976) 751–767. https://doi.org/10.1107/S0567739476001551.
[43] A. Harabor, P. Rotaru, N.A. Harabor, P. Nozar, A. Rotaru, Orthorhombic YBCO-123 ceramic oxide superconductor: Structural, resistive and thermal properties, Ceram. Int. 45 (2019) 2899–2907. https://doi.org/10.1016/j.ceramint.2018.07.272.
[44] B.L.F. Brito, J. Dweck, Reuse of kaolinitic waste as a precursor of pozzolanic material, J. Therm. Anal. Calorim. 147 (2022) 6087–6097. https://doi.org/10.1007/s10973-021-10957-2.
[45] J. Kuczek, M. Szumera, D. Rutkowska-Zbik, M. Gackowski, J. Sułowska, Thermal and spectroscopic behavior of glasses from P2O5–SiO2–K2O–MgO–CaO–Co2O3 system, J. Therm. Anal. Calorim. (2022). https://doi.org/10.1007/s10973-022-11362-z.
[46] A. Kumar, K.A. Ramisetty, S. Bordignon, B.K. Hodnett, P. Davern, S. Hudson, Preparation, stabilisation, isolation and tableting of valsartan nanoparticles using a semi-continuous carrier particle mediated process, Int. J. Pharm. 597 (2021) 120199. https://doi.org/10.1016/j.ijpharm.2021.120199.
[47] L. Sciascia, S. Casella, G. Cavallaro, G. Lazzara, S. Milioto, F. Princivalle, F. Parisi, Olive mill wastewaters decontamination based on organo-nano-clay composites, Thermophys. Asp. Funct. Ceram. Surf. 45 (2019) 2751–2759. https://doi.org/10.1016/j.ceramint.2018.08.155.
[48] F. Parisi, F. Bernardini, G. Cavallaro, L. Mancini, S. Milioto, D. Prokop, G. Lazzara, Halloysite nanotubes/pluronic nanocomposites for waterlogged archeological wood: thermal stability and X-ray microtomography, J. Therm. Anal. Calorim. 141 (2020) 981–989. https://doi.org/10.1007/s10973-020-09637-4.

Declaration of interests

☒ The authors declare that they have no known competing financial interests or personal relationships that could have appeared to influence the work reported in this paper.

☐The authors declare the following financial interests/personal relationships which may be considered as potential competing interests: